Plasma Sources Science and Technology

Production of hydrogen negative ions in an ECR volume source: Balance between vibrational excitation and ionization

To cite this article before publication: Spyridon Aleiferis *et al* 2018 *Plasma Sources Sci. Technol.* in press https://doi.org/10.1088/1361-6595/aabf1b

Production of hydrogen negative ions in an ECR volume source: Balance between vibrational excitation and ionization

S Aleiferis[1,2,*], P Svarnas[1]†, S Béchu[2], O Tarvainen[3], and M Bacal[4]

[1]High Voltage Laboratory, Electrical and Computer Engineering Department, University of Patras, Rion-Patras, 26504, Greece

[2]LPSC, Université Grenoble-Alpes, CNRS/IN2P3, 53, Avenue des Martyrs, F-38026, France

[3]Departement of Physics, University of Jyväskylä, 40500 Jyväskylä, Finland

[4]UPMC, LPP, Ecole Polytechnique, Palaiseau, Université PARIS-SUD 11, UMR CNRS 7648, France

†E-mail : svarnas@ece.upatras.gr

Abstract

The operation of an ECR-driven (2.45 GHz) hydrogen negative ion source is studied. Electron densities and temperatures are investigated with electrostatic probes and negative ion densities are measured with laser photodetachment. Vacuum ultraviolet irradiance measurements are focused on molecular transitions to the ground state while high-resolution visible emission spectroscopy is used to study the transitions between excited states for both molecules and atoms. The standalone operation of the source is found to be more efficient in higher pressures (12 mTorr) where negative ion densities are as high as $4\text{x}10^9$ cm^{-3}. Further investigation on the operation of the source reveals a rich vibrational spectrum. On the other hand, a limitation on the production of negative ions which is attributed to a lack of low-energy electrons becomes apparent. The underlying mechanisms that lead to this behavior are discussed along with possible solutions to this issue. Finally, the rates of different negative ion destruction processes are estimated and compared.

*Current address: a) EUROfusion Consortium, JET, Culham Science Centre, Abington, OX14 3DB,UK, b) Fusion Technology Group, National Centre for Scientific Research 'Demokritos', 15310 Aghia Paraskevi, Athens, Greece

1. Introduction

The operation of next generation fusion experiments like ITER, relies on Neutral Beam Injection (NBI) systems for the heating and current drive of fusion plasmas [1]. These systems should be able to produce hydrogen or deuterium beams with particle energies in the excess of 1 MeV [2]. In earlier NBI systems, positive ions were accelerated and then neutralized in a gas cell to produce the neutral beams [3]. However, the neutralization efficiency of positive ions is reduced to negligible values in the MeV energy range [3]. On the other hand, the gas cell neutralization efficiency of negative ions remains acceptable (~60%) for such or even higher energies[3]. Additionally, for negative ion beams, various proposals have been made, for photodetachment-based neutralization systems with expected neutralization efficiencies above 90% [4]. Based on these characteristics, negative ions are nowadays considered as a prerequisite for the future of fusion research [5].

Presently, efficient negative ion sources rely on the so-called surface production process or, in other words, the surface ionization of hydrogen atoms and positive ions [6]. For this process to be efficient, evaporation of cesium is required, in order to reduce the work function of the production surface [6]. Even though the use of cesium allows negative ion sources to reach ITER specifications [7], it is related with a variety of problems including difficulties in maintenance and unstable operation [8]. Thus, avoiding cesium usage would be highly desirable.

Another efficient source of negative ions in a hydrogen discharge comes from the bulk of the plasma, where the volume production mechanism takes place. While different processes might be responsible for the formation of negative ions [9], the volume production mechanism mainly refers to the efficient process of dissociative attachment (DA) of low-energy (cold) electrons to vibrationally excited molecules [6]:

$$H_2(v)+e(<1eV)\rightarrow H^-+H \qquad (1)$$

Contrary to surface production sources, volume production sources operate with pure hydrogen, having the practical advantage of inherently cesium-free operation, which makes them an attractive choice. However, as it becomes obvious from the cross section of the process [10], DA is very sensitive to both electron and vibrational kinetics, which in turn may be affected by a variety of parameters. Vibrational kinetics refer to reactions that vibrationally excite or deactivate molecules. An effective way for molecule excitation to high vibrational levels is related to excitation to singlet electronic states, followed by spontaneous radiative decay back to the ground state (E-V excitation) [11]. Depending on the operational parameters and the design of the ion source, an additional important source of vibrational states is the recombinative desorption of atoms on the surface of various materials [11]. The complexity with which the above reactions are combined makes the prediction of the behavior of negative ion sources quite difficult and their development very challenging.

At the same time, H^- negative ions have low electron affinity (0.75 eV) [12], and thus collisions in the bulk of the plasma with a variety of particles may destroy them [13]. There are, however, three processes of primary importance: a) mutual neutralization (MN) during collisions with positive ions (Reaction (2)), b) collisions with neutral particles from which the associative detachment (AD) (Reaction (3)) is the most prominent for cold plasmas and c) electron detachment (ED) during collisions with energetic electrons.

$$H^- + H^+, H_2^+, H_3^+ \rightarrow H + ... \quad (2)$$

$$H^- + H \rightarrow H_2 + e \quad (3)$$

$$H^- + e \rightarrow H + e + e \quad (4)$$

Reaction (2) has a total rate coefficient which is about 1.3x10^{-7} (300/T$_g$)$^{1/2}$ for the H$^+$ positive ion, 1.0x10^{-6} (300/T$_g$)$^{1/2}$ for the H_2^+ positive ion and 1.0x10^{-6} (300/T$_g$)$^{1/2}$ for the H_3^+ positive ion [14,15]. The rate coefficient of Reaction (3) is approximately 1.3x10^{-9} cm^{3}s^{-1}[15] and finally the loss rate due to Reaction (4) needs to be calculated using the available cross section[16] and the estimated or measured electron temperature. In the above references T_g stands for the gas temperature which is considered similar to the ion temperature. Gas temperature refers here to the translational temperature of the species that participate in each reaction. Furthermore, it is reminded that the reaction rates depend as well on the species densities.

In this work, the production and destruction of H$^-$ negative ions in the Electron Cyclotron Resonance (ECR) negative ion source "Prometheus I" [9,17] is investigated. The study employs a combination of diagnostics including electrostatic probes, laser photodetachment, visible emission spectroscopy and Vacuum-Ultraviolet (VUV) irradiance measurements. In order to detect how the injected power is shared by various processes, the power dependence of the source operation is investigated with the above diagnostics. Apart from a general characterization of the source, the primary finding of the present study is a limitation of the production of H$^-$, imposed by an unbalanced production of the reactants of DA, i.e. cold electrons and vibrationally excited molecules. Experimental data indicate that the underlying cause of this behavior is related to the employed electron heating scheme, and on this basis, possible ways to overcome this limitation are discussed. On the other hand, among the various H$^-$ ion destruction mechanisms, associative detachment appears here to be dominant.

This paper is organized in the following manner. The experimental setup and diagnostics are described in Section 2. In Section 3 the experimental results are presented and discussed, focusing on the mechanisms of ion production and destruction which are responsible for the behavior of the source. Finally, the main conclusions of this study are summarized in Section 4.

2. Experimental Setup

2.1 The source Prometheus I

In **Figure 1** a conceptual diagram of the source Prometheus I is presented. It consists of a cubic (24 cm inner edge) stainless steel chamber with the necessary viewports for plasma diagnostics. The plasma is sustained by a 2D network of ECR plasma elementary sources [18]. Each elementary source is driven by an independent microwave solid-state power supply (2.45 GHz) able to provide up to 180 W. A tuner embedded on the main body of each source, is used for impedance matching which maximizes the microwave power absorbed by the plasma [19]. The impedance matching is manually optimized in order to reduce microwave power reflection (maximum accepted value 5 W). The elementary sources and their power supplies are cooled by water which is circulated by a water-cooling system (CoolMaster K-003.6).

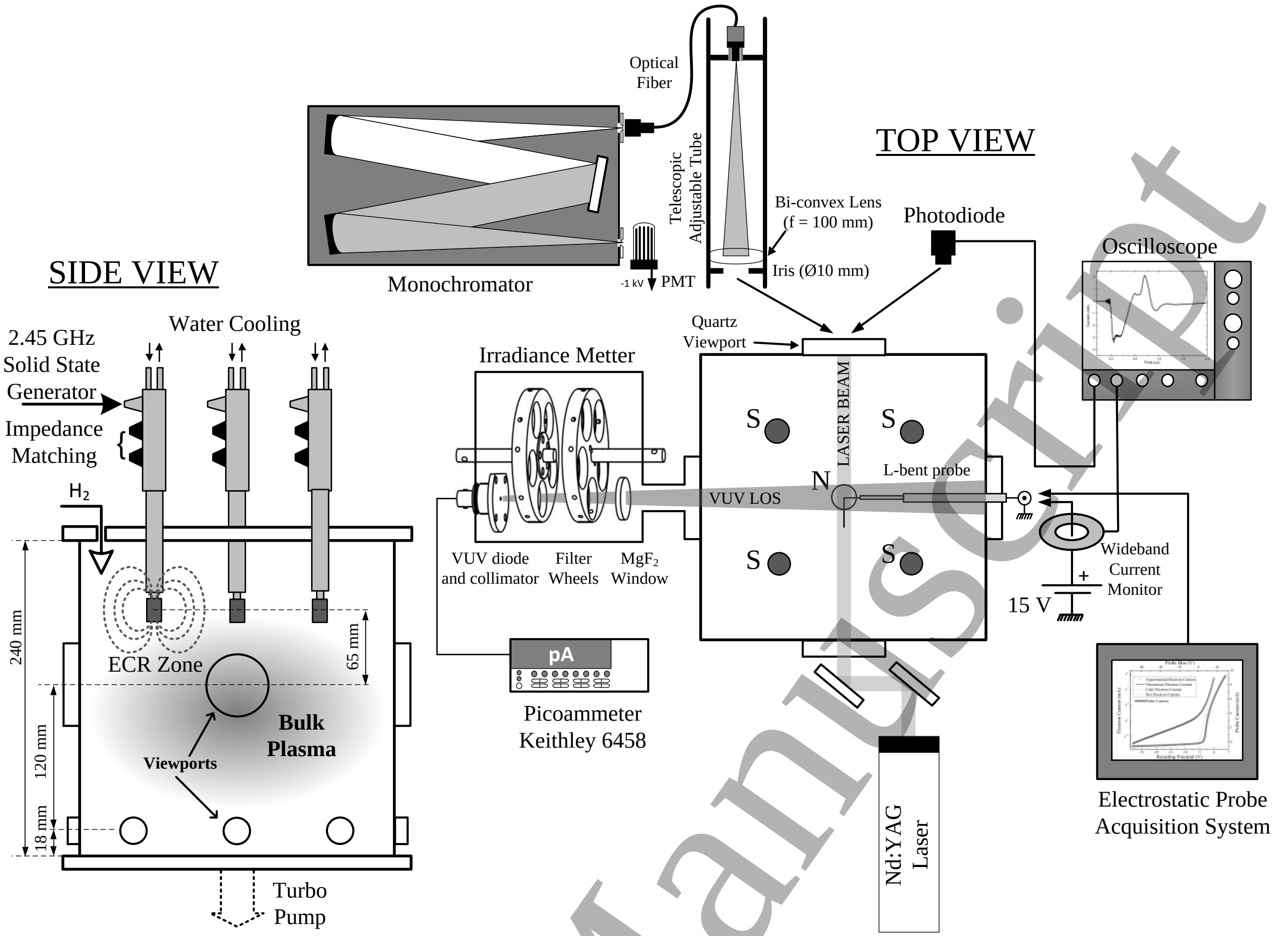

Figure 1. Experimental setup of the source Prometheus I with the installed diagnostics: electrostatic probe, photodetachment, visible emission spectroscopy and VUV irradiance measurements.

A turbomolecular pump adapted under the bottom flange evacuates the source down to $3x10^{-6}$ Torr. Pure H_2 (N50) is introduced by a digital mass flow controller (MKS 1179B) at a flow rate between 2.1 and 23.2 sccm. The working pressure varies respectively between 1 and 20 mTorr (filling gas pressure), and it is accurately monitored with an absolute pressure transducer (MKS Baratron 627D). The discharge is operated with flowing neutral gas with a typical duration for a complete gas renewal being approximately 0.5-1 s, typically exceeding the characteristic equilibration times in the plasma. Therefore, the only effect the continuous gas flow has on the stationary plasma equilibrium is to prevent impurities from building-up[20]. For the present experiments, three pressure values are investigated (4, 8 and 12 mTorr).

The operation of the elementary plasma sources is described in detail by Lacoste et al [21]. Briefly, each one consists of two parts: a cylindrical samarium-cobalt (Sm_2Co_{17}) permanent magnet, magnetized along its axis, and a coaxial line parallel to the magnetization vector, having an open end at the rear pole of the magnet. The microwave power can thus be transmitted through the plasma and be mostly absorbed near the region where the ECR condition is fulfilled. For the microwave frequency of 2.45 GHz, the required magnetic field is 875 G [21]. The ECR regions are indicated in **Figure 2(a)**, where the magnetic flux contours of the magnetic field created by the five permanent magnets are presented along the diagonal cut-plane (see figure inset). The ECR surfaces correspond to the inner contours around each magnet (bold lines). The calculation of the magnetic field is here realized with the ACDC module of the COMSOL Myltiphysics® numerical suite.

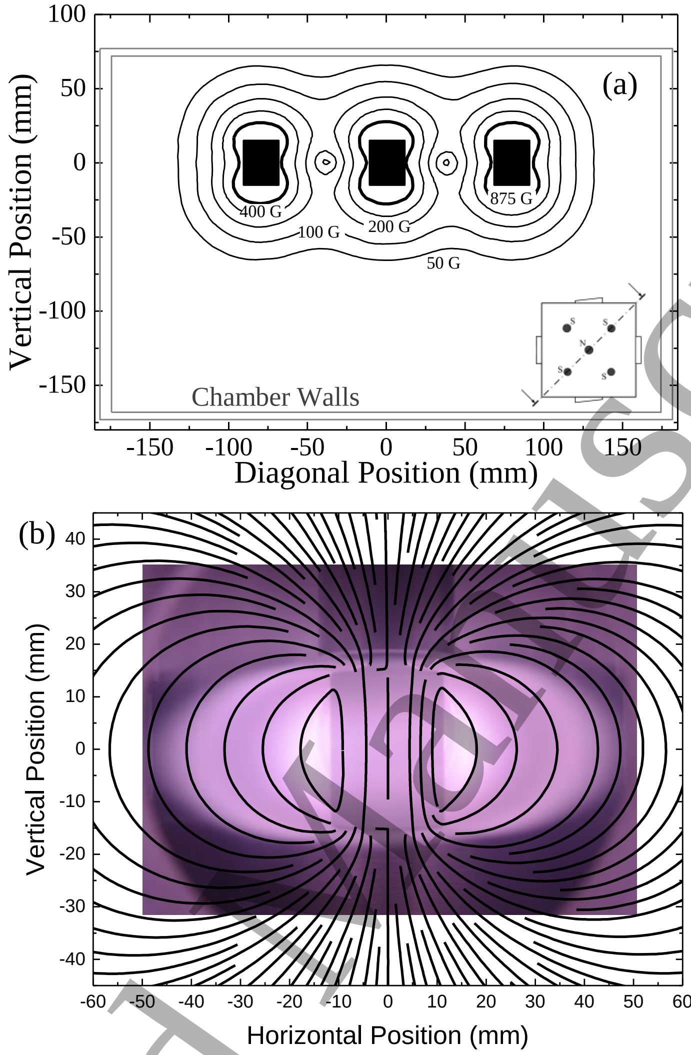

Figure 2. Static magnetic field created by the permanent magnets. **(a)** Contours of the magnetic field along the diagonal cut-plane shown in the inset. **(b)** Streamlines of the magnetic field, superimposed on a photograph of an operating elementary source.

The streamlines of the magnetic field are presented in **Figure 2(b)** superimposed on a photograph of an operating source. The high-energy (hot) electrons which gain their energy in the ECR zones appear to be mostly confined within the luminous regions in the vicinity of the permanent magnet, whereas the plasma diffuses outwards roughly perpendicularly to the magnetic field (strictly speaking, it is assumed here that the plasma is ionizing, i.e. the excitation and de-excitation states are in balance, and thus the light emission profile matches the profile of the hot electrons). In other words, with this configuration, the ECR magnetic field also plays the role of the magnetic filter, allowing only cold electrons to diffuse into the bulk plasma region (**Figure 1**).

2.2 EEDF Measurements

A cylindrical tungsten electrostatic probe is immersed in the plasma as presented in **Figure 1**. The probe is made from a 0.25 mm in diameter tungsten wire and the tip (exposed to the plasma) is L-bent in order to be aligned with the laser beam for the photodetachment measurements. The tip is 15 mm in total length with the bent part being 11 mm. The rest of the wire is housed in a telescopic configuration of dielectrics (alumina tube inside a wider quartz tube) that insulates and protects it from the plasma. The quartz tube is supported inside a stainless steel tube that ends in a standard BNC vacuum feedthrough. A CF flange-to-quick connect coupling adapter makes a vacuum joint with the steel tube and at the same time allows the linear translation of the probe.

The acquisition of electrostatic probe current-voltage (I-V) curves is accomplished with a custom-made system described elsewhere [22]. Each measurement procedure includes 10 s of probe cleaning by electron current-induced incandescence followed by another 10 s of cooling-down. The acquisition is realized point by point in steps of approximately 100 mV. For each point 2^{12}-2^{13} voltage-current samples are averaged in order to reduce plasma-induced noise.

At the probe position, the magnetic field of the ECR modules has vertical downward direction and a magnitude of 51 Gauss, while the probe tip itself is oriented horizontally (i.e. perpendicular to the magnetic field). The lowest electron temperature observed during the present experiments is about 0.5 eV which corresponds to an electron Larmor radius of about 0.34 mm. Thus, even in the worst case, the probe radius (0.125 mm) is sufficiently smaller than the electron Larmor radius, validating the use of the "classical" non-magnetized probe theory [23,24].

Typical plasma parameters, i.e. floating and plasma potential, electron densities and temperatures, are obtained from numerical treatment and fitting procedures on the I-V curve data [25]. More specifically, plasma potential is estimated as the maximum of the I-V curve first derivative and positive ion current is linearly extrapolated from high retarding potentials and subtracted from the I-V curve. The remaining current (electron current) is fitted as the sum of two exponentials, as shown in **Figure 3(a)**, which corresponds to a bi-Maxwellian Electron Energy Distribution Function (EEDF). The experimental EEDF is derived from the second derivative of the probe total current (Druyvesteyn method) [24]. **Figure 3(b)** demonstrates how well the experimental EEDF is described by the bi-Maxwellian distribution derived from the fitting procedure.

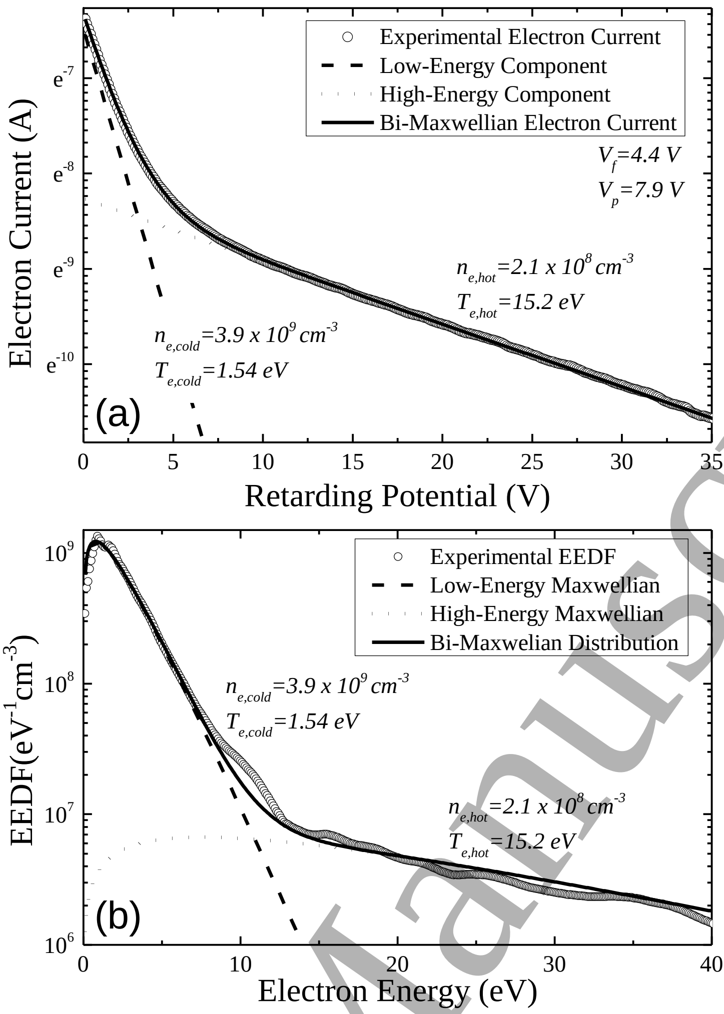

Figure 3. Typical electrostatic probe measurement (180 W/elementary source; 4 mTorr). **(a)** Fitting of the electron current as the sum of two exponential functions for the determination of electron densities and temperatures for the cold and hot electrons.**(b)** Experimental EEDF derived by the Druyvesteyn method and compared with the synthesized EEDF, corresponding to (a).

2.3 H^- negative ion density measurements

The photodetachment diagnostic technique with one laser beam is used for the determination of the negative ion absolute density [26]. Briefly, a short (~5 ns) Nd:YAG 1064 nm laser pulse, generated from a Quantel Brilliant EaZy (330 mJ/pulse) unit, is concentrically aligned with the bent part of the probe tip and detaches the extra electron of negative ions inside the irradiated cylindrical volume. The excess (i.e. photodetached) electrons, in the section of the irradiated volume that contains the bent part of the probe tip, sharply increase the electron current collected by the positively biased probe. A typical photodetachment current pulse is presented in **Figure 4**. The density of negative ions can then be calculated from the amplitude of the current pulse as explained in [26]. To avoid any potential errors that arise from the use of the traditional capacitive decoupling circuit [27], a wideband current transformer (Pearson electronics 6585; 400 Hz - 200 MHz), connected directly to a digital oscilloscope (LeCroyWaveSurfer 104Xs-A; 1GHz/5GSample s^{-1}), is used to measure the transient current pulse due to the photodetached electrons.

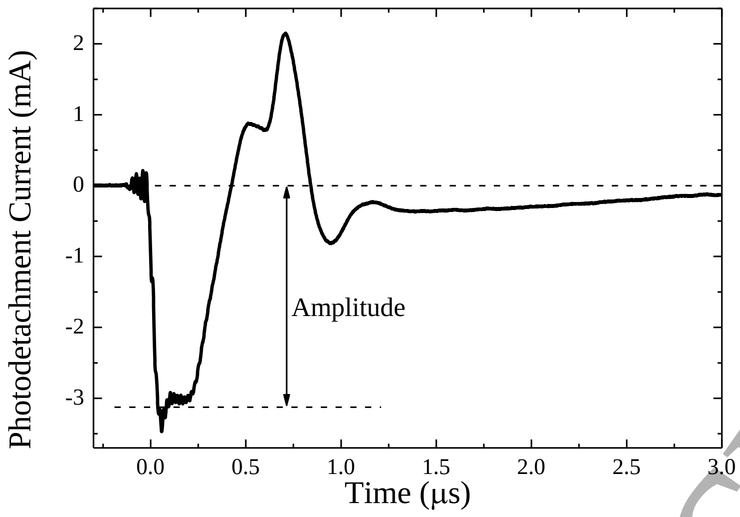

Figure 4. Typical photodetachment current pulse at 180 W/elementary source and 11 mTorr.

Various parameters of the photodetachment diagnostic technique are properly set for its valid application[26,28]. Firstly, the laser radius is chosen to be 3 mm which sufficiently exceeds the probe collection radius (~0.1 mm which is the typical Debye length for the present experimental conditions). Secondly, the probe bias has been set to +15 V (i.e. 7-8V above plasma potential) which is sufficient for collecting all the detached electrons without causing the incandescence of the probe tip due to electron current. To establish this, a series of measurements was realized which demonstrated that a +15 V bias leads to the saturation of the photodetached electron current [26,28]. Lastly, the energy density of the laser beam is chosen to be around 70 mJ cm^{-2} which is high enough to destroy all the negative ions in the irradiated volume. This is ensured by the saturation of the photodetachment signal while the latter is being recorded versus the increasing laser power (see references [26,28] for details on the proper application of the photodetachment technique).

2.4 Evaluation of the gas composition

Optical emission spectroscopy is employed for the evaluation of the atomic and molecular absolute densities under various operating conditions. The process demands the estimation of the atomic temperature, the molecular temperature and the degree of dissociation. The concept followed and the related setup, are both explained in this section. The distinction between atomic and molecular temperatures, instead of a common gas temperature, is justified below based on our results and references where similar findings are reported. The main concept is that atoms gain energy in dissociation but do not distribute all the released energy in collisions and thus have different temperature than the molecules.

Accordingly, a motorized monochromator (Jobin-Yvon THR 1000) having focal length of 1 m is used. It is equipped with a holographic grating (170-750 nm; 2400 grooves/mm) and the SpectrAcq2 (JobinYvon) driving/acquisition system. Absolute wavelength calibration is realized with an Hg(Ar) pencil-style lamp (6035 Newport Corp.). The light is efficiently guided into the monochromator with an optical fiber (Ceramoptec UV 1500/1590N) adapted on an optical matcher and detected by an electron photomultiplier tube (Hamamatsu

R928; 185-900 nm). In order to collect the light mainly from the bulk plasma, a bi-convex lens is used to focus the light from the center of the chamber into the entrance of the optical fiber. The lens is adapted inside a telescopic tube to allow focusing at the center of the chamber. The measured spectra are calibrated in terms of relative intensity. This is achieved by employing a quartz-tungsten-halogen lamp (Newport 6333; 3300 K color temperature at 12 V dc bias).

The emissions of interest, in the visible range, are the Balmer series (H_α: transition n = 3 → n = 2 and H_β: transition n = 4 → n = 2) of atomic hydrogen and the molecular Fulcher-*α* band (triplet transition $d^3\Pi_u \rightarrow a^3\Sigma_g^+$). It is just here reminded that molecules have degrees of freedom of three types (translation, vibration and rotation) and the energy distribution governing each of them in equilibrium is associated with a corresponding temperature.

- Among the various emissions of the Fulcher-*α* system, the Q-branches are of particular importance, as they have been previously used for the determination of the **molecular temperature** [29,30]. The first step of this process is the determination of the rotational temperature T^*_{rot} of the upper level of the transition ($d^3\Pi_u$). The measured intensities (I_J) of the lines presented in **Figure 5(a)** are directly linked to T^*_{rot} through the relation [29]:

$$\ln\left(\frac{\lambda^4 I_J}{S_J}\right) = \frac{-B_v J\left(J+1\right)hc}{kT^*_{rot}} + const \qquad (5)$$

where λ is the wavelength of the emission, S_J is the line strength, B_v is the rotational constant of the excited state, J is the rotational quantum number, h and k are the Planck and Boltzmann constants, respectively, and c is the speed of light. The line strength is calculated from the Höln-London formula: S_J=0.5(2J+1)(2t+1) with t = 0 for even J and t = 1 for odd J. The rotational temperature T^*_{rot} is obtained from the slope of the Boltzmann plot (**Figure 5(b)**).

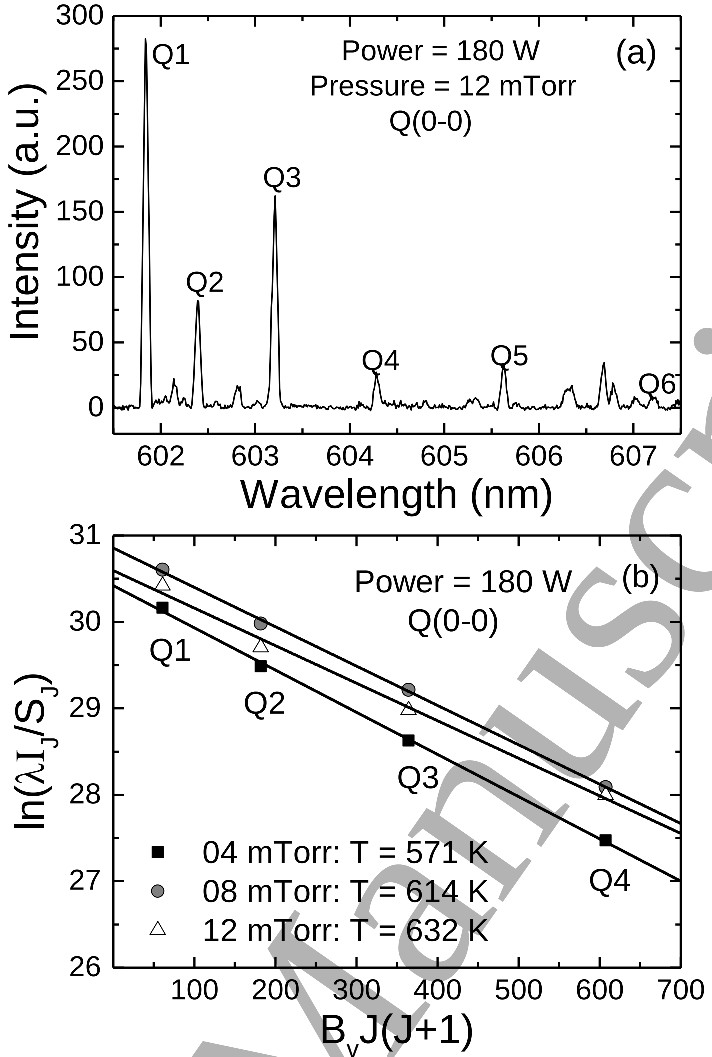

Figure 5. **(a)** Indicative spectrum of the Q-branch of the 0-0 band of the Fulcher-*α* system **(b)** Indicative Boltzmann plots corresponding to the line intensities of (a). The rotational temperature is determined with linear fitting. The temperature values in the inset refer to the corresponding molecular ground state translational temperatures.

Under the low pressure conditions of the present study, a Boltzmann rotational distribution with temperature T_{rot}^{0} in the ground electronic state of the molecules images to a Boltzmann rotational distribution with temperature T_{rot}^{*} in the excited electronic state [31]. In this case, the ratio of the two temperatures is given by the ratio of the respective rotational constants B_v^* and B_v^0 of the two levels. For the ground state the rotational constant is $B_v^0 = 60.809$ cm^{-1}[31] whereas for the excited level $d^3\Pi_u$ it is $B_v^* = 30.364$ cm^{-1}[31]. Thus, the translational temperature of the molecules, which is equal to the ground electronic state rotational temperature, is approximated by the relation [30,32]:

$$T_{H_2} \approx T_{rot}^{0} \approx \frac{B_v^*}{B_v^0} T_{rot}^{*} \approx 2T_{rot}^{*} \qquad (6)$$

- A typical raw spectrum of the second Balmer line (H_β) is presented in **Figure 6(a)** and is used for the evaluation of the **atomic temperature**, following processes similar with those proposed in references [33] and [34].

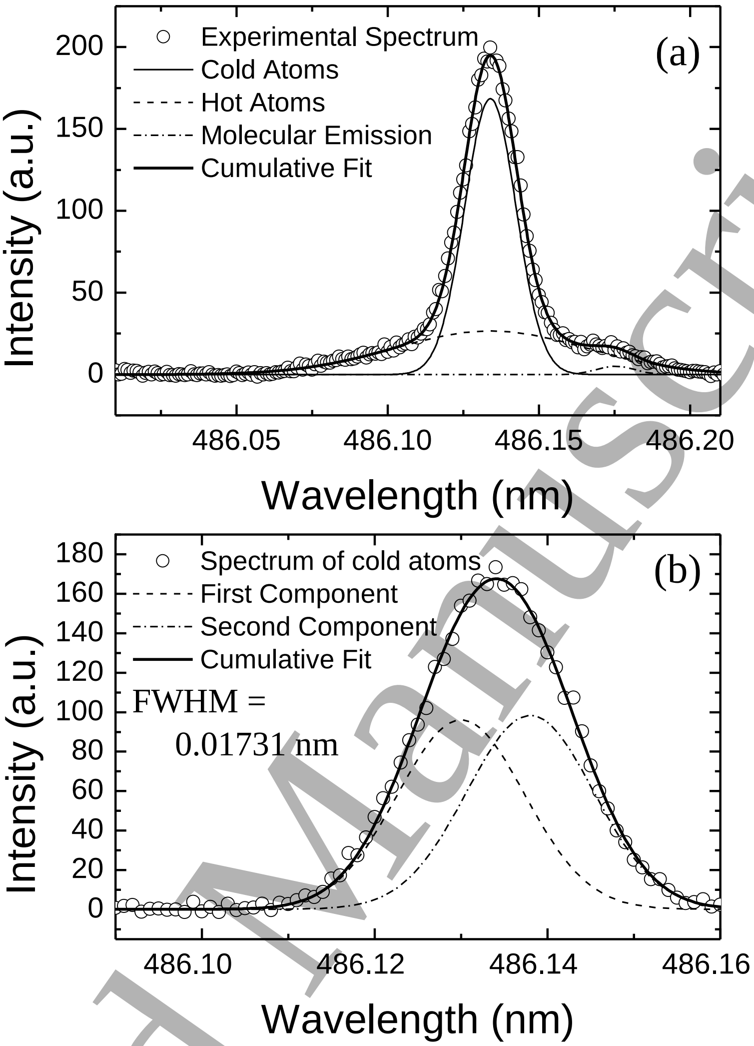

Figure 6. (a) Typical raw spectrum of the H_β atomic line. The line shape implies the presence of two hydrogen populations (hot and cold atoms). **(b)** H_β line that corresponds solely to direct excitation from ground state atomic hydrogen (cold population). A synthetic spectrum calculated with the two barycentres, fitting a typical residual experimental spectrum.

The raw spectrum is structured by various components due to different mechanisms that create H(n=4) atoms. A central narrow component must be introduced to account for the main body of hydrogen cold atoms, while a wider component ("wings") must be introduced to account for energetic (hot) atoms created during the dissociative processes [34,35]. The translational temperature of the cold atoms is equal to that of the H(n=4) atoms that are created through direct excitation [34] and it can be evaluated from the central component of the H_β spectrum. The mathematical treatment of the emission line profile requires an assumption on the atomic distribution and Maxwellian one is adopted to evaluate the “effective temperature” of the cold population. Thus, the atomic line spectrum is approximated with a tri-Gaussian function as presented in **Figure 6(a)**. Apart from the two above components, the third weak component corresponds to an irrelevant molecular emission at 486.17 nm [36].

The Gaussian functions gave also the best fit following numerical tests with different possible functions, like Voigt profile. Thus, we mainly deal here with Doppler broadening effect. Additionally, in the region of measurements, the plasma density (see below) is in the order of 10^{10} cm^{-3}, i.e. too low to make Stark broadening prevailing [37]. Pure Gaussian functions can be further justified by the bibliography for plasmas running under close to the present conditions, where line profiles with same shapes have been obtained [31]. Similarly, in reference [38] Stark, van de Waals, and resonance broadening are negligible.

Consequently, the two theoretical Gaussian functions that correspond to emission by hot atoms and molecules are subtracted, and the residual experimental spectrum (open cycles in **Figure 6(b)**) which corresponds to direct excitation of ground state atoms is used for the determination of the translational temperature (in kelvins) of the atomic hydrogen, according to the following formula [34]:

$$T_H = \left(\frac{\Delta\lambda_{Doppler}}{\lambda} \frac{1}{716 \times 10^{-9}} \right)^2 \quad (7)$$

where λ is the central wavelength of the atomic line and $\Delta\lambda_{Doppler}$ stands for the atomic line broadening.

Before the atomic translational temperature calculation, two corrections should be made. The first refers to line broadening due to the fine structure of the residual experimental atomic line and the second to the instrumental broadening. For the first correction, up to seven components may be taken into account [32], but the line may be well approximated by two barycentres only, as proposed by Tomasini et al [34] and seen in **Figure 6(b)**. The two barycentres share the same broadening and are separated by 77 mÅ, which corresponds the fine structure separation for the H_β line [35]. For the second correction, the typical instrumental broadening is evaluated with a HeNe laser (Oriel 79288, 633 nm, 4 mW). For the 20 μm slits used, it is measured to be equal to 0.0086 nm. We acknowledge the fact that the wavelength of this laser is higher than the wavelength of the line under study and the instrumental broadening at lower wavelength is slightly larger. Nevertheless, another laser was not available and it is implied that the atomic temperatures calculated represent the upper limit. However, the discrepancy between the molecular and atomic temperatures cannot be explained by the instrumental broadening alone (see section 3.1).

- For the determination of the ratio of the atomic to molecular density (n_H/n_{H2}) or the **degree of dissociation** ($D = n_H/(n_H+2n_{H2})$), components from both the molecular and atomic spectrum are required. The spectra in this case have to be interpreted using a simple collisional-radiative model as the one developed by Lavrov et al [39,40]. This model calculates the degree of dissociation based on the ratio of the first two lines of the Balmer series (H_α and H_β) to the Q_1 line of the 2-2 band of the Fulcher-α system (hereafter $F(2\text{-}2)Q_1$). The central wavelengths of the above emissions are 656.283, 486.134 and 622.481 nm, respectively. The model uses as well as parameters the molecular translational temperature and the temperature of high energy electrons, which are both measured here as it is explained above.

The composition of the hydrogen plasma mainly refers to neutral atoms and molecules in their electronic ground state, short-lived electronically excited atomic and molecular species, metastables which mostly relate to H(1s) and $H_2(c^3\Pi_u)$ [41], and of course charged particles. Firstly, for the present pressure range, the neutral particle density is in the order of 10^{14} cm^{-3}, whereas the density of the plasma is in the order of 10^9 – 10^{10} cm^{-3}, giving a degree of ionization in the order of 10^{-4} – 10^{-5}. At the same time the upper limit for the total density of the metastable neutrals has been investigated by Komppula et al [41] and has been found to be approximately 0.5% of the neutral gas density for a similar ECR discharge. Thus the pressure (p), as it is measured by the Baratron which is installed as close as about 5 cm to the chamber, is approximately equal to the sum of the partial pressures for the two gaseous species (i.e. atoms and molecules) based on the Dalton's law:

$$p \cong n_H k_B T_H + n_{H_2} k_B T_{H_2} \qquad (8)$$

where k_B = 1.037x10^{-16} mTorr cm^3 K^{-1} is Boltzmann's constant, n_H and n_{H2} are the atomic and molecular densities, respectively, and T_H and T_{H2} are the atomic and molecular translational temperatures, respectively. Using the measured translational temperatures and the calculated dissociation degree, the absolute values of atomic and molecular densities can be estimated from **Equation (8)**.

2.5 Rough approach of VDFs by means of VUV emission spectroscopy

Discussion on the H^- ion production mechanisms requires information on the vibrational distribution function (VDF). The measurement of VDF would require absorption spectroscopy techniques which are not applied here. Alternatively, VUV emission measurements may lead indirectly to reliable data for supporting such a discussion. Towards this direction, the irradiance meter described in detail by Komppula et al [41] is used. Briefly, the device is based on an SXUV photodiode (IRD-incSXUV20BNC) with a responsivity of about 0.02 A/W in the VUV range. The photodiode current is measured with a digital pico-ammeter (Keithley 6458). Due to an iris adapted in front of the photodiode, the light is collected from a conic line of sight with an included angle of 4.6°.Using a filter wheel, band-pass filters centered at characteristic emissions of hydrogen plasma, are placed in front of the photodiode (**Figure 1**). For this study a filter centered on the intense part of the Lyman band emission at 161 nm with a FWHM of 20 nm is used. The transmittance of the filter is presented in **Figure 7** (curve measured by Komppula et al [41]), on top of a typical VUV spectrum obtained with a VUV spectrometer (McPherson Model 234/302). From this figure, it becomes obvious that the light that passes from the filter is dominated by the Lyman band emission. The VUV irradiance meter is chosen instead of the VUV spectrometer due to its higher signal-to-noise (SNR) ratio, especially for low power conditions.

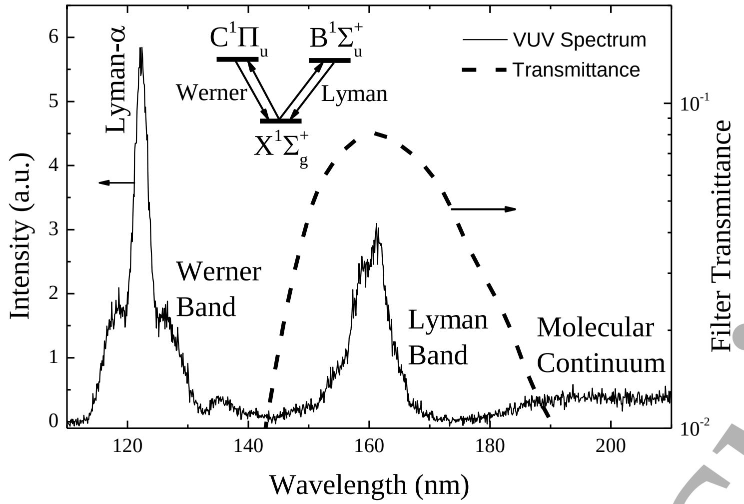

Figure 7. Lyman-band filter transmittance [41] on top of a typical VUV spectrum of Prometheus I in the ECR zone of the central elementary source.

The measurement of the Lyman-band is very important because of its relation with the vibrational excitation of the gas. Lyman-band is emitted during the decay of the $B^1\Sigma_u^+$ singlet, which together with the decay from the $C^1\Sigma_u^+$ singlet, is the main source of vibrationally excited molecules of a hydrogen discharge (EV excitation)[11].The transitions from the $B^1\Sigma_u^+$ singlet back to the ground state are optically allowed and, thus, its lifetime is in the order of ns [42]. At the same time, the measured irradiance includes the most intense part of Lyman-band which accounts for the majority of irradiance. Furthermore, the contribution of cascade effects from upper singlet states on the measured emission can be considered small in comparison to the effect of direct excitation to the $B^1\Sigma_u^+$ state. Thus, it may be argued that the irradiance is proportional to the excitation rate to the $B^1\Sigma_u^+$ singlet.

It would be very useful to have additional data on VDFs. While the full vibrational spectrum would be difficult to be measured (requiring techniques like Laser Induced Fluorescence [43]), a more simplified approached is possible, based on the available data here. If the VDF is approached as a Maxwellian function, it can be described by the total molecular density (n_{H2}) and a vibrational temperature (T_{vib}). Based on this assumption, the Lyman-band irradiance (I_{LB}), which as explained above is proportional to the excitation rate of the singlet $B^1\Sigma_u^+$,is given from the relation:

$$I_{LB} \propto \sum_{v=0}^{14} n_{H_2(v)} n_e \left\langle \sigma_{XB}(v) u \right\rangle = K\left(T_{vib}, T_{e,hot}\right) n_{H_2} n_{e,hot} \qquad (9)$$

where $n_{H2(v)}$ is the density of each vibration level of the ground state, $\sigma_{XB}(v)$ is the cross section of $B^1\Sigma_u^+$ singlet excitation, u is the velocity of electrons, and $n_{e,hot}$ and $T_{e,hot}$ are the density and temperature of the hot electron population, respectively. In the last part of this equation, only the hot electron population is taken into account because of the high threshold of the excitation cross section which is in the excess of 10 eV. Based on **Equation (9)** and the parameters measured according to sections 2.2 and 2.4, T_{vib} can be evaluated using the available

$B^1\Sigma_u^+$ singlet excitation cross sections[16]. Since the Lyman-band irradiance is not measured in absolute units, the absolute value of the vibrational temperature is not accessible, but quite informative qualitative results are unveiled. Furthermore, the region of Lyman-band that is probed is related with transitions to higher vibrational levels only[44]. As a result, the effective vibrational temperature that is measured here refers mostly to those levels and it is not representative of the entire VDF. Nevertheless, the information that is revealed is still useful, since the higher vibrational levels are mainly responsible for the production of negative ions[45] and, consequently, of greater interest for this work.

3. Results

3.1 Plasma Characterization with respect to H^- ion production

When a source is intended for fusion, it is expected to require high power input. In this case it is very important for the operation of the source (i.e. the production of negative ions) to scale up with power in an efficient manner. This necessitates the deposition of the injected power to the processes that contribute the most to the production of negative ions, without wasting it on stray processes. In order to investigate the power deposition, the power dependence of a variety of parameters is probed with the above diagnostics.

The power dependence of electron densities and temperatures is presented in **Figure 8**. It is observed that the cold electron population (**Figure 8a** and **8c**) evolves with power in a significantly different manner for the case of low pressure (4 mTorr). For higher pressures (8 and 12 mTorr), the electron density increases monotonically for the entire power range. On the other hand, for the lower pressure, the density reaches a maximum at about 120 W and starts decreasing after this value. At the same time, while for the higher pressures electron temperature retains values lower than 0.8 eV which are appropriate for the production of negative ions, for the case of 4 mTorr the temperature increases considerably reaching values as high as 1.5 eV. It appears that the cold electron population at higher pressures is more favorable for the production of negative ions.

Regarding the hot electron population, one can observe that they have a density (**Figure 8b**) which is about two orders of magnitude lower. However, the high temperature of these electrons, being about 15 eV (**Figure 8d**), makes them very important for the production of negative ions as they contribute to the ionization and excitation processes that create the precursors of negative ions, i.e. cold electrons and vibrationally excited molecules respectively. Noteworthy is the fact that the hot electron temperature seems to be almost independent of both pressure and power.

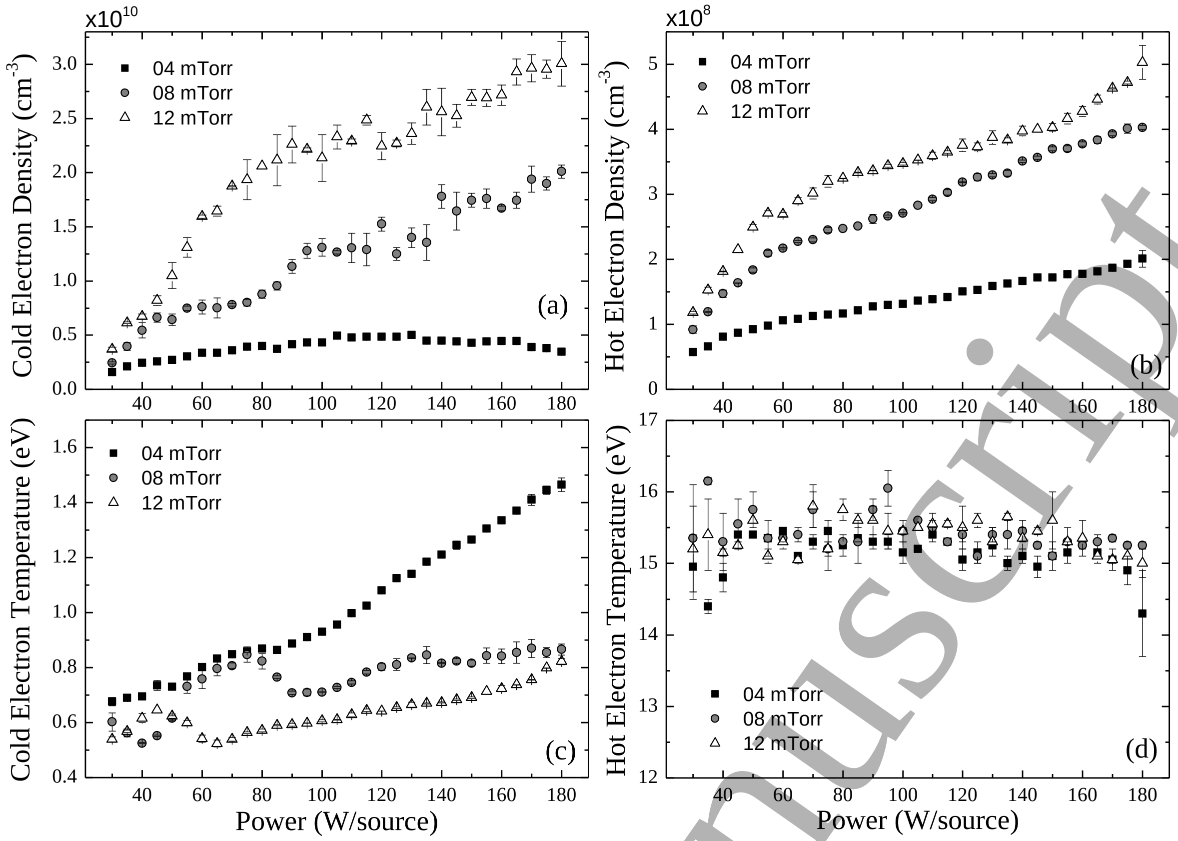

Figure 8. Power dependence of electron densities and temperatures.**(a)** Cold electron density; **(b)** Hot electron density; **(c)** Cold electron temperature; **(d)** Hot electron temperature.

The measured negative ion density is presented in **Figure 9**, where three different behaviors are observed. For the higher pressure of 12 mTorr, the negative ion density seems to scale up well with power, having only a slight tendency for saturation and reaching values as high as $4x10^9$ cm^{-3}. For 8 mTorr, the saturation is more dramatic limiting the negative ion density to values of about $2x10^9$ cm^{-3}. Finally, for the case of 4 mTorr, the negative ion density has a maximum at a power of about 100-110 W, after which it starts decreasing, behaving much like the density of cold electrons. Naturally, since electrons are one of the reactants of dissociative attachment which produces the negative ions, this similarity indicates that the density of cold electrons limits negative ion production. However, understanding the underlying mechanisms that lead to this behavior requires additional experimental data (see below). Nevertheless, it is obvious that the saturation observed here limits the power scaling of the source when working in the low pressure regime, which is nowadays a prerequisite for neutral beam injection (maximum specification for ITER 2.25mTorr [2]), and thus this limitation deserves to be further investigated.

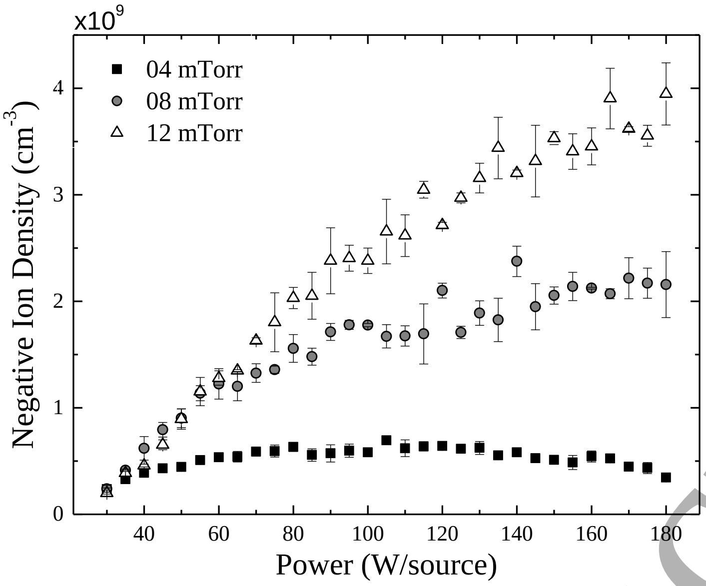

Figure 9. Power dependence of negative ion density.

Using the irradiance meter, the total emission of Lyman-band is measured. The results presented in **Figure 10** show no sign of saturation, indicating that the power is efficiently deposited on excitation processes. While the irradiance measurement directly probes the rate of vibrational heating of the gas, it provides no additional information about the vibrational distribution or the vibrational temperature. However, using **Equation (9)**, the vibrational temperature can be estimated, providing more information about the production of negative ions.

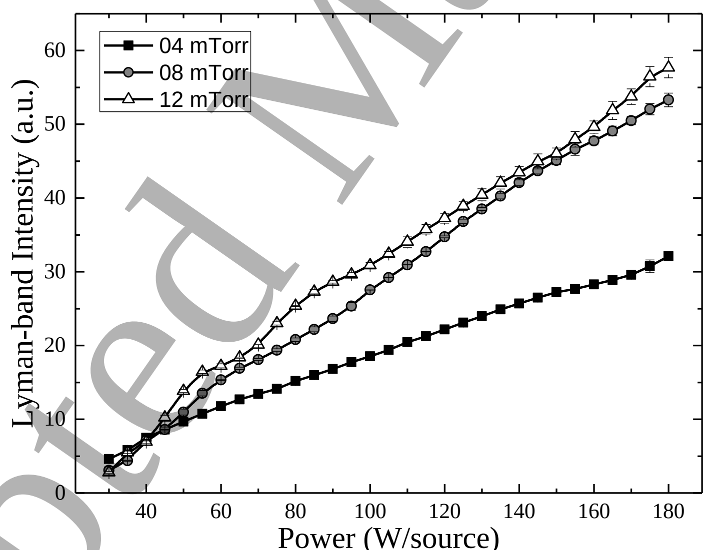

Figure 10. Power dependence of Lyman-band irradiance.

Since the hot electron temperature is experimentally found to be almost constant and equal to 15 eV (**Figure 8d**), the rate coefficient $K(T_{vib}, T_{e,hot})$ of **Equation (9)** becomes a function of the vibrational temperature and the following proportionality holds true:

$$K\left(T_{vib}\right) \propto \frac{I_{LB}}{n_{H_2} n_{e,hot}} \tag{10}$$

This rate coefficient of the $B^1\Sigma_u^+$ singlet excitation from the ground state is calculated and presented as a function of the vibrational temperature of the ground state in **Figure 11**. The dependence on the vibrational temperature for the range which is of interest for the production of negative ions [46], is monotonic, allowing a qualitative estimation of the relative vibrational temperature.

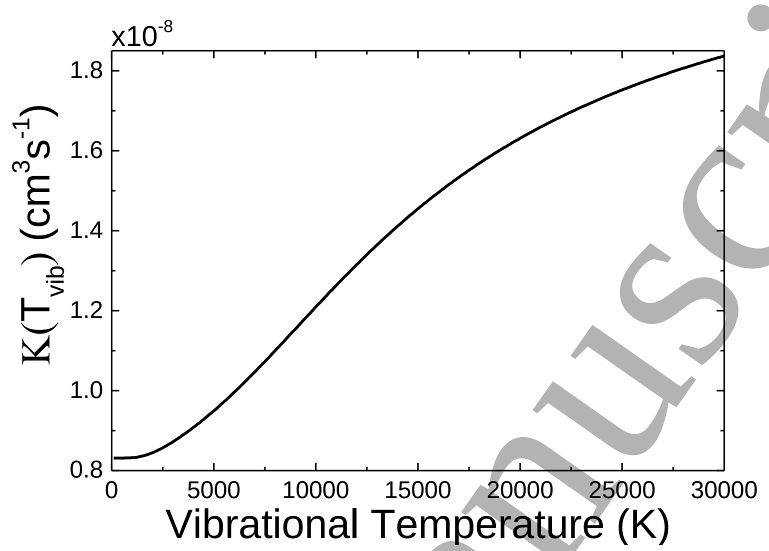

Figure 11. Dependence of $B^1\Sigma_u^+$ singlet excitation rate coefficient on vibrational temperature.

The Lyman-band intensity and the hot electron density, which are required by **Equation (10)** are already measured. Using the spectroscopic techniques described in the section 2.4 and **Equation (8)**, the molecular density n_{H2} can be calculated as well. For this, the molecular and atomic temperatures are measured and presented in **Figure 12**. The molecular part of the gas remains relatively cold, reaching temperatures slightly greater than 600 K. On the other hand, the translational temperature of atoms is much greater than the temperature of molecules and it spans the range 1400-1900 K. This important difference has already been reported in the bibliography. Tomasini et al. [34] used high-resolution Fourier transformer spectroscopy and showed that the H atom kinetic temperature is higher than the H_2 one, in microwave plasmas of low pressure. They reported temperatures of 620-1430 K and 800-1170 K, respectively, depending on the power and position of measurements. Amorim et al. [47] found H atom temperatures as high as 1600 K in the positive column of a DC discharge, whereas the molecular temperature was close to 300 K, with a degree of dissociation much less than 1%. Samuell and Corr [48] studied a radiofrequency helicon discharge (<10 mTorr) using spectroscopic techniques, and they claimed that the atomic and molecular species were not found to be in thermal equilibrium, with the atomic temperature being mostly larger than the molecular temperature. In low power operation like in the present work (<1 kW), the molecular hydrogen temperature was observed to be linearly proportional to the pressure while the atomic hydrogen temperature was inversely proportional. Both temperatures were observed to rise linearly with the input power. For this low power regime, they measured molecular and atomic temperatures up to about 475 K and 1300 K, respectively, depending on the pressure.

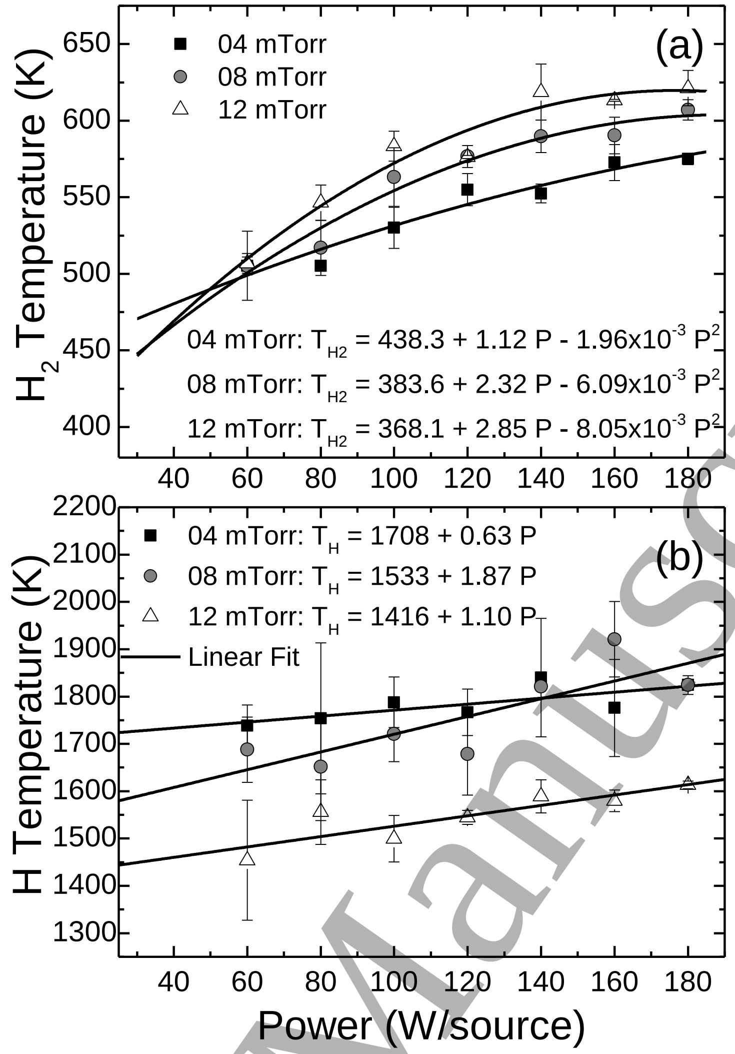

Figure 12. Translational temperature of **(a)** molecules and **(b)** atoms as a function of power. For the easement of later calculations, experimental data in (a) and (b) are fitted by square and linear functions, respectively.

Finally, the ratio of atomic to molecular density is presented in **Figure 13**. The degree of dissociation increases as a function of power, imposing an additional limit to the power scaling for two reasons: (i) an increasing density of atoms leads to higher rates of associative detachment, which is responsible for a major part of the loss rate of negative ions and (ii) the molecules that are dissociated are no longer available for dissociative attachment of electrons possibly leading to the reduction of the negative ion formation rate. A possible way to overcome this limitation would be to incorporate in the source appropriate materials in order to recycle these atoms back into molecules with their ro-vibrational energy being as high as possible [11]. A wide range of investigations on this subjects may be referred [11,49,50].

The absolute molecular and atomic densities, which are estimated using **Equation (8)**, are presented in **Figure 14**. The reduction of the molecular density as a function of power is attributed to the heating of the molecules (**Figure 12**(**a**)), whereas the atomic density actually increases with power. The same increase versus power takes place for the molecular continuum emission (**Figure 7**) (curve not shown here). The triplet excitation resulting in the emission of molecular continuum and dissociation of the molecule, is considered the main dissociation channel for hydrogen plasmas [41]. Thus, the increasing atomic density can be attributed to the increasing irradiance of the molecular continuum which is measured by placing an additional VUV filter (**Figure 1**).

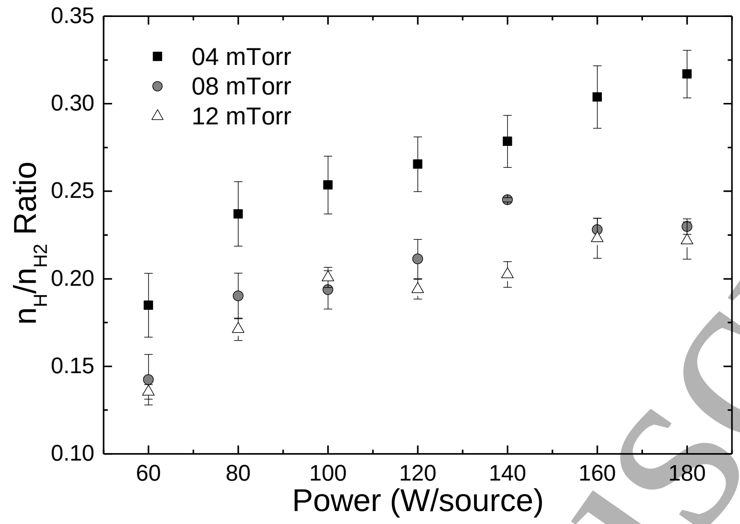

Figure 13. Power dependence of the ratio of atomic-to-molecular density.

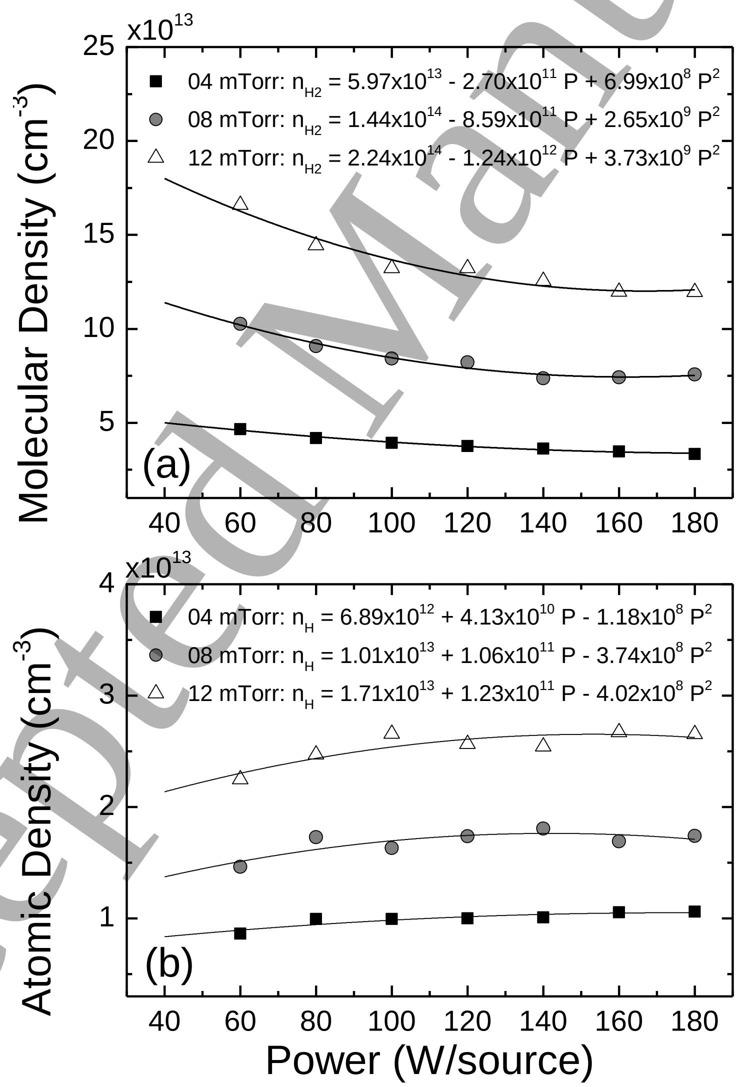

Figure 14. Power dependence of **(a)** molecular and **(b)** atomic densities. For the easement of later calculations, both density values have been fitted by square functions.

By introducing the estimated molecular density in **Equation (10)**, the $B^1\Sigma_u^+$ singlet excitation rate can be estimated in arbitrary units (**Figure 15**). It can be observed that the vibrational temperature is monotonically increasing. This is in agreement with the result of the power dependence of the Lyman-band irradiance presented in **Figure 10**, which indicates the efficient vibrational heating of the gas in the Prometheus I source.

The case of 4 mTorr, for which the cold electron density and the negative ion density scale up inefficiently with power, demonstrates a considerably higher vibrational temperature. As it is explained above, the limitation on the negative ion production appears to be imposed by the cold electron density. Nevertheless, the calculated vibrational temperatures demonstrate that the same discharge has a very rich vibrational spectrum which remains largely unexploited due to the insufficient density of cold electrons.

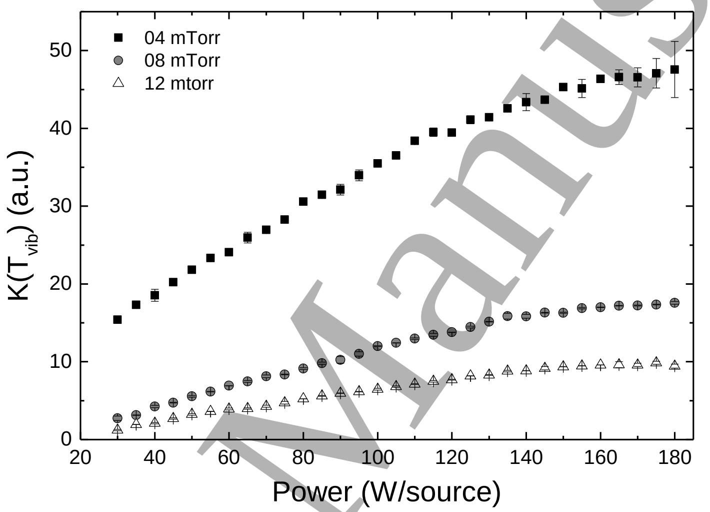

Figure 15.Power dependence of the excitation rate coefficient for the $B^1\Sigma_u^+$singlet.

3.2 H⁻ ion production in respect to DA

In general, the formation rate which is attributed to dissociative attachment depends on the EEDF and the VDF in a way that is determined by the cross section of the process. By considering Maxwellian distributions, the formation rate can be calculated in an effective manner. In this case, the formation rate is expressed by the equation:

$$\left(\frac{dn_-}{dt}\right)_+ = \sum_{v=0}^{14} n_{H_2}(v) n_e \langle \sigma_{DA}(v), u \rangle = K_{DA}(T_{vib}, T_{e,cold}) n_{e,cold} n_{H_2} \qquad (11)$$

where n_- is the negative ion density, $(dn_-/dt)_+$ is the formation rate, n_e is the electron density, $n_{H2}(v)$ is the vibrationally-resolved molecular density and $\sigma_{DA}(v)$ the vibrationally-resolved dissociative attachment cross section. The production rate is investigated herein using the last part of **Equation (11)**, where only the cold electron population is taken into account since DA is a low energy electron impact process. Here, $K_{DA}(T_{vib}, T_{e,cold})$ is the effective rate coefficient which depends on the vibrational temperature and cold electron temperature, $n_{e,cold}$ is the cold electron density, and n_{H2} is the total molecular density. The rate coefficient K_{DA} is calculated using the available cross section [15] and its values are presented in **Figure 16**.

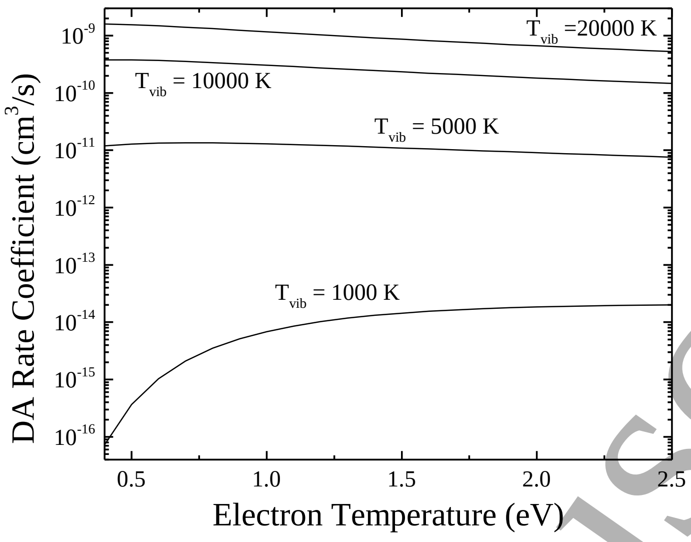

Figure 16. Total rate coefficient K_{DA} as a function of electron temperature, for various vibrational temperatures. The cross sections used for this calculations are from reference [16].

It would be useful to determine which of the four variables of **Equation (11)** dominates. **Figure 16** shows that K_{DA} is more sensitive to the vibrational temperature than to the electron temperature. At the same time, **Figure 14(a)** shows that n_{H2} decreases as a function of power. This could in part explain the limited power scaling of the source for H^- production at lower pressures. However, in the same figure, for higher pressures a steeper reduction of n_{H2} versus power is observed, without leading to limitations for H^- production. This fact suggests that $n_{e,cold}$ is the second defining parameter in **Equation (11)**. Two more conclusions may be drawn: (i) **Figure 15** shows that higher vibrational levels are populated versus power, especially at lower pressures, compensating the reduction of the total H_2 density; (ii) the increased vibrational excitation at lower pressures and the reduced H^- production suggests once more that $n_{e,col}$ is a critical parameter.

It would be quite interesting to show the operational windows of the source in terms of H^- ion production on a plane defined by the two parameters that have been found to be crucial (cold electron density and $B^1\Sigma_u^+$ singlet excitation rate coefficient in the place of vibrational temperature). This pattern is given in **Figure 17**, where the negative ion density is color-coded. Evidently, increasing electron density by operating in higher pressures benefits the production of negative ions but, for analyzing the full information of this pattern, the processes of ionization and vibrational excitation need to be considered, as follows.

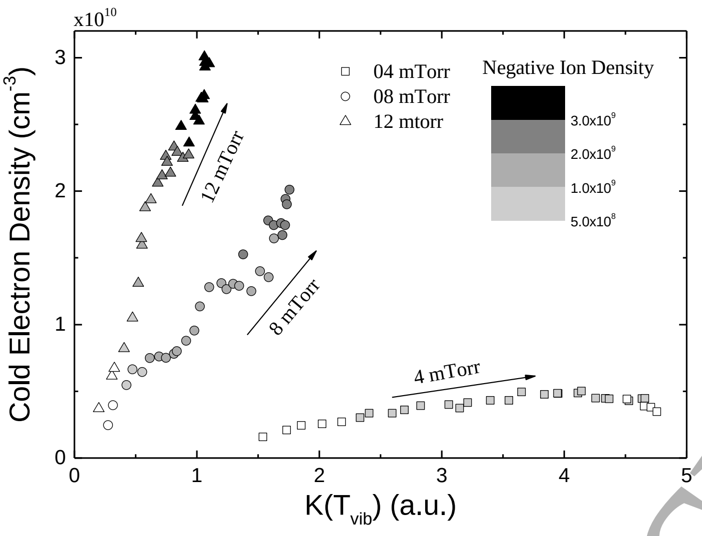

Figure 17. Color-coded negative ion density on the plane of electron density versus vibrational temperature. Instead of the actual vibrational temperature, the rate coefficient $K(T_{vib})$ is used.

The main ionization channel for hydrogen plasmas is non-dissociative ionization[16]. The vibrationally-resolved cross section of this process is found in reference [16]. For these qualitative calculations, the energy threshold of this ionization is assumed to be the ionization threshold of the first vibrational level (15.42 eV), reduced by the difference in vibrational energy between the considered levels. On the other hand, the excitation processes to the $B^1\Sigma_u^+$ and $C^1\Sigma_u^+$ singlet states are considered as the main vibrational heating processes. These transitions account for about 80% of the EV excitations [51], which is the main production channel of high vibrational states. Both the ionization and excitation processes are attributed to collisions of hot electrons with hydrogen molecules and it makes thus sense to directly compare the rate coefficients of these processes with the hot electron energy as parameter, as presented in **Figure 18**.

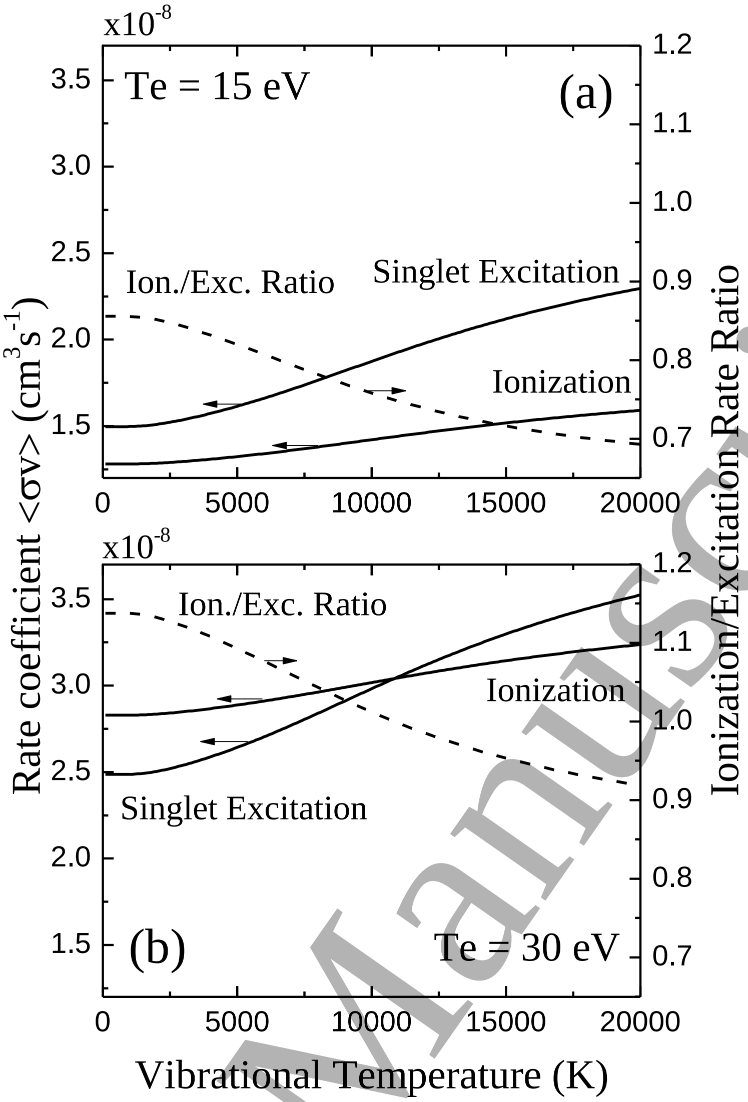

Figure 18. Rate coefficients of singlet excitation and ionization processes, for electron temperature of **(a)** 15 eV and **(b)** 30 eV. Cross sections are from [16].

Obviously, vibrational temperature enhances both processes. However, singlet excitation seems to be the process that better exploits the vibrational heating, which means that, as the vibrational temperature increases, vibrational heating is increasingly favored. For the temperature of 15 eV that was measured in our source this "cascade" phenomenon promotes vibrational heating instead of ionization. This explains why the rate of vibrational heating, a measure of which is the Lyman-band irradiance of **Figure 10**, is monotonically increasing, while the electron density saturates or even decreases as a function of power.

The rate coefficient calculation of **Figure 18**(**b)** is included in order to demonstrate how the balance between ionization and vibrational excitation might be controlled by the hot electron temperature. Vibrational excitation seems to be favored because singlet excitation has a slightly lower energy threshold [16]. However, once an electron has enough energy, it is more probable to ionize than to excite the molecule [52]. This is why, for an electron temperature of 30 eV, the two processes are more evenly balanced, even if vibrational heating is still favored at high vibrational temperatures.

A better balance between these two processes is established when the present source is operated with higher pressure, due to the reduced vibrational temperature; this is obviously the operation which leads to higher negative ions densities (accumulated darker points in **Figure 17**). However, by increasing the pressure in order to reduce the vibrational temperature, one treats high vibrational temperatures as undesirable. On the contrary, highly ro-vibrationally excited molecules are desirable, and it is hence here necessary to increase the cold electron density. Concepts may be found in references [53,54], but this source improvement is beyond the scope of the present work.

3.3 Plasma characterization with respect to H^- ion destruction

The analysis so far is concentrated on the H^- production mechanisms. However, the steady state density of negative ions which is measured is determined by the equilibrium between formation and loss processes. Thus, it is very important to know the loss rate and the effect it has on the measured density.

Using the obtained results, the contribution of each destruction process to the total loss rate can be calculated. The first contribution is from MN (see Reaction (1)). Unfortunately, no data is available for the percentage of the atomic and molecular positive ions for this particular plasma generator. However, the total plasma density is measured with the electrostatic probe. In that case an effective rate coefficient for all MN processes might be estimated by assuming that the ratio of atomic to molecular ions would be similar to the ratio of neutral atoms to neutral molecules which is already measured. This is also supported by experimental evidence, which verified that in typical hydrogen discharges each molecule experiences on average several tens of ionization and excitation processes and several dissociation processes during the time it spends in the plasma chamber [41]. The second contribution is AD (see Reaction (2)) and presents no challenge since the atomic density is already estimated. Finally, for ED (See reaction (3)), a simplification might be made based on the acquired data. Because of its high energy threshold, only the hot electron population contributes to electron detachment [16]. For the almost constant temperature of the hot electron population (15 eV) a rate coefficient can be calculated instead of integrating each EEDF. The rate coefficient which is calculated from the available cross section with a 15 eV electron temperature is 1.55×10^{-6} $cm^3 s^{-1}$. The loss rates for the three different pressures are calculated and presented in **Figure 19**.

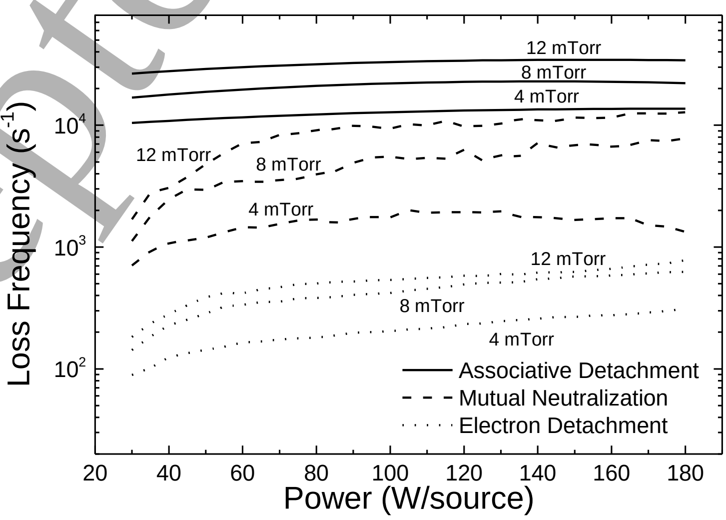

Figure 19. Power dependence of the loss frequencies that correspond to the main destruction processes MN, AD, and ED.

Evidently, the dominant destruction process is associative detachment from collisions with atoms. This can be attributed to the high dissociation degree of the source (about 12% for this source compared with 3% for typical filament sources [20]). The different dissociation degree is most likely due to the different EEDFs in the two discharge types, favoring triplet state excitation and subsequent dissociation in the case of microwave heating as discussed in reference [55]. Mutual neutralization is another important loss process being about three times lower than dissociative attachment. Finally, electron detachment, being about two orders of magnitude lower, could fairly be ignored. This is due to the low density of hot electrons in the bulk of the plasma. This also proves that the magnetic field of the ECR elementary sources plays efficiently the role of the magnetic filter, by confining hot electrons in the vicinity of these sources.

An important note is that, the power dependence of the loss processes does not explain the decrease of the H^- ion density with increasing power at 4 mTorr (compare **Figure 9** and **19**), leaving thus principally the production processes (presented above) to be responsible for the behavior of the negative ion density.

4. Conclusions

The ECR (2.45 GHz) H^- negative ion source "Prometheus I" was studied in terms of volume production of H^- negative ions. The source was found to operate more efficiently in the high pressure regime (12 mTorr) for which negative ion density reached values as high as $4x10^9$ cm^{-3}. For the lower pressure (4 mTorr), negative ion density was reduced and, more importantly, scaled up poorly with power. Additionally, following a qualitative analysis, it was concluded that the specific ECR discharges promote vibrational heating of the gas instead of ionization. A similar conclusion was reached for another microwave source [41], indicating that this might be a more general limitation of ECR sources. However, any generalization requires a wider consideration of the involved phenomena. Consequently, the stand-alone operation of the source was limited by the availability of sufficiently cold electrons, especially in the low pressure regime. For higher pressures, the vibrational temperature was reduced but a better balance was achieved between ionization and excitation processes, which created cold electrons and negative ions by dissociative attachment, respectively. At the same time, the efficient vibrational heating of the gas in the low pressure regime should not be considered as a drawback in terms of H^- negative ion production. On the contrary, this is a prerequisite for H^- ion production through dissociative attachment, as long as the ionization can be increased in a controlled manner. The potentiality for an independent enrichment of the source with cold electrons will be the topic of future studies.

Acknowledgements

The present work was partially supported by the Andreas Metzelopoulos Scholarships of the University of Patras.

References

[1] Speth E, Falter H ., Franzen P, Fantz U, Bandyopadhyay M, Christ S, Encheva A, Fröschle M, Holtum D, Heinemann B, Kraus W, Lorenz A, Martens C, McNeely P, Obermayer S, Riedl R, Süss R, Tanga A, Wilhelm R and Wünderlich D 2006 Overview of the RF source development programme at IPP Garching *Nucl. Fusion* **46** S220–38

[2] Hemsworth R, Decamps H, Graceffa J, Schunke B, Tanaka M, Dremel M, Tanga A, De Esch H P L, Geli F, Milnes J, Inoue T, Marcuzzi D, Sonato P and Zaccaria P 2009 Status of the ITER heating neutral beam system *Nucl. Fusion* **49** 045006

[3] Hemsworth R S and Inoue T 2005 Positive and negative ion sources for magnetic fusion *IEEE Trans. Plasma Sci.* **33** 1799–813

[4] McAdams R 2014 Beyond ITER: Neutral beams for a demonstration fusion reactor (DEMO) *Rev. Sci. Instrum.* **85** 02B319

[5] Jianglong W, Yahong X, Lizhen L, Yuming G, Wei Y, Jun L, Chundong H, Yuanlai X, Jiang Caichao, Ling T, Peng S and Yongjian X 2016 Design of the Prototype Negative Ion Source for Neutral Beam Injector at ASIPP *Plasma Sci. Technol.* **18** 954

[6] Bacal M and Wada M 2015 Negative hydrogen ion production mechanisms *Appl. Phys. Rev.* **2** 021305

[7] Franzen P and Fantz U 2014 On the NBI system for substantial current drive in a fusion power plant: Status and R&D needs for ion source and laser neutralizer *Fusion Eng. Des.* **89** 2594–605

[8] Santoso J, Manoharan R, O'Byrne S and Corr C S 2015 Negative hydrogen ion production in a helicon plasma source *Phys. Plasmas* **22** 093513

[9] Aleiferis S, Tarvainen O, Svarnas P, Bacal M and Béchu S 2016 Experimental investigation of the relation between H^- negative ion density and Lyman-α emission intensity in a microwave discharge *J. Phys. Appl. Phys.* **49** 095203

[10] Wadehra J M 1984 Dissociative attachment to rovibrationally excited H_2 *Phys. Rev. A* **29** 106–10

[11] Mario Capitelli, Roberto Celiberto, Gianpiero Colonna, Fabrizio Esposito, Claudine Gorse, Khaled Hassouni, Annarita Laricchiuta, Savino Longo and Mario Capitelli 2016 *Fundamental aspects of plasma chemical physics: Kinetics* (New York: Springer)

[12] Zhang H 1999 *Ion sources* (New York: Springer)

[13] Bacal M 2006 Physics aspects of negative ion sources *Nucl. Fusion* **46** S250–9

[14] Hjartarson A T, Thorsteinsson E G and Gudmundsson J T 2010 Low pressure hydrogen discharges diluted with argon explored using a global model *Plasma Sources Sci. Technol.* **19** 065008

[15] Matveyev A A and Silakov V P 1995 Kinetic processes in a highly-ionized non-equilibrium hydrogen plasma *Plasma Sources Sci. Technol.* **4** 606–17

[16] Janev R K, Reiter D and Samm U 2003 *Collision Processes in Low-Temperature Hydrogen Plasmas* (Institut für Plasmaphysik)

[17] Aleiferis S, Svarnas P, Tsiroudis I, Béchu S, Bacal M and Lacoste A 2014 H^- Negative Ion Production From a 2D Network of ECR Dipolar Plasma Sources *IEEE Trans. Plasma Sci.* **42** 2828–9

[18] Latrasse L, Lacoste A, Sirou J and Pelletier J 2007 High density distributed microwave plasma sources in a matrix configuration: concept, design and performance *Plasma Sources Sci. Technol.* **16** 7–12

[19] Baële P, Béchu S, Bès A, Pelletier J and Lacoste A 2014 An open-ended coaxial plasma source with extended operating parameters: plasma impedance, coupling and energy efficiency *Plasma Sources Sci. Technol.* **23** 064006

[20] Mosbach T 2005 Population dynamics of molecular hydrogen and formation of negative hydrogen ions in a magnetically confined low temperature plasma *Plasma Sources Sci. Technol.* **14** 610–22

[21] Béchu S, Soum-Glaude A, Bès A, Lacoste A, Svarnas P, Aleiferis S, Ivanov A A and Bacal M 2013 Multi-dipolar microwave plasmas and their application to negative ion production *Phys. Plasmas* **20** 101601

[22] Aleiferis S and Svarnas P 2014 Automated electrostatic probe device of high resolution and accuracy *Rev. Sci. Instrum.* **85** 123504

[23] Aanesland A, Bredin J, Chabert P and Godyak V 2012 Electron energy distribution function and plasma parameters across magnetic filters *Appl. Phys. Lett.* **100** 044102

[24] Godyak V A and Demidov V I 2011 Probe measurements of electron-energy distributions in plasmas: what can we measure and how can we achieve reliable results? *J. Phys. Appl. Phys.* **44** 233001

[25] Hershkowitz N 1989 How Langmuir Probes Work *Plasma Diagnostics: Volume 1, Discharge Parameters and Chemistry* ed O Auciello and D Flamm (San Diego: Academic Press) p 113

[26] Bacal M 2000 Photodetachment diagnostic techniques for measuring negative ion densities and temperatures in plasmas *Rev. Sci. Instrum.* **71** 3981

[27] Bryant P M and Bradley J W 2013 Optimum circuit design for the detection of laser photodetachment signals *Plasma Sources Sci. Technol.* **22** 015014

[28] Christ-Koch S, Fantz U, Berger M and NNBI Team 2009 Laser photodetachment on a high power, low pressure rf-driven negative hydrogen ion source *Plasma Sources Sci. Technol.* **18** 025003

[29] Iordanova S 2008 Spectroscopic temperature measurements in hydrogen inductively-driven plasmas at low pressures *J. Phys. Conf. Ser.* **113** 012005

[30] Iordanova S, Koleva I and Paunska T 2011 Hydrogen Degree of Dissociation in a Low Pressure Tandem Plasma Source *Spectrosc. Lett.* **44** 8–16

[31] Qing Z, Otorbaev D K, Brussaard G J H, van de Sanden M C M and Schram D C 1996 Diagnostics of the magnetized low-pressure hydrogen plasma jet: Molecular regime *J. Appl. Phys.* **80** 1312–24

[32] B. P. Lavrov 1978 Relation between the rotational temperature and gas temperature in a low-pressure molecular plasma *Sov. Tech. Phys. Lett.* **4** 574–5

[33] Tatarova E, Felizardo E, Dias F M, Lino da Silva M, Ferreira C M and Gordiets B 2009 Hot and super-hot hydrogen atoms in microwave plasma *Appl. Phys. Lett.* **95** 181503

[34] Tomasini L, Rousseau A, Gousset G and Leprince P 1996 Spectroscopic temperature measurements in a microwave discharge *J. Phys. Appl. Phys.* **29** 1006–13

[35] Péalat M, Taran J-P E, Bacal M and Hillion F 1985 Rovibrational molecular populations, atoms, and negative ions in H2 and D2 magnetic multicusp discharges *J. Chem. Phys.* **82** 4943

[36] Bruneteau A M, Hollos G, Bacal M and Bretagne J 1990 Temperature and relative density of atomic hydrogen in a multicusp H− volume source *J. Appl. Phys.* **67** 7254

[37] Huddlestone R H and Leonard S L 1965 *Plasma Diagnostic Techniques* (Academic Press)

[38] Oliveira C, Souza Corrêa J A, Gomes M P, Sismanoglu B N and Amorim J 2008 Hyperthermal hydrogen atoms in argon-hydrogen atmospheric pressure microplasma jet *Appl. Phys. Lett.* **93** 041503

[39] Lavrov B P, Pipa A V and Röpcke J 2006 On determination of the degree of dissociation of hydrogen in non-equilibrium plasmas by means of emission spectroscopy: I. The collision-radiative model and numerical experiments *Plasma Sources Sci. Technol.* **15** 135–46

[40] Lavrov B P, Lang N, Pipa A V and Röpcke J 2006 On determination of the degree of dissociation of hydrogen in non-equilibrium plasmas by means of emission spectroscopy: II. Experimental verification *Plasma Sources Sci. Technol.* **15** 147–55

[41] Komppula J, Tarvainen O, Kalvas T, Koivisto H, Kronholm R, Laulainen J and Myllyperkiö P 2015 VUV irradiance measurement of a 2.45 GHz microwave-driven hydrogen discharge *J. Phys. Appl. Phys.* **48** 365201

[42] Astashkevich S A and Lavrov B P 2002 Lifetimes of the electronic-vibrational-rotational states of hydrogen molecule (Review) *Opt. Spectrosc.* **92** 818–50

[43] Gabriel O, Schram D C and Engeln R 2008 Formation and relaxation of rovibrationally excited H_2 molecules due to plasma-surface interaction *Phys. Rev. E* **78**

[44] Dabrowski I 1984 The Lyman and Werner bands of H2 *Can. J. Phys.* **62** 1639–64

[45] Svarnas P, Breton J, Bacal M and Mosbach T 2006 Pressure optimization for H^- ion production in an electron cyclotron resonance-driven and a filamented source *Rev. Sci. Instrum.* **77** 03A532

[46] Taccogna F, Schneider R, Longo S and Capitelli M 2007 Modeling of a negative ion source. I. Gas kinetics and dynamics in the expansion region *Phys. Plasmas* **14** 073503

[47] Amorim J, Baravian G, Touzeau M and Jolly J 1994 Two-photon laser induced fluorescence and amplified spontaneous emission atom concentration measurements in O2 and H2 discharges *J. Appl. Phys.* **76** 1487

[48] Samuell C M and Corr C S 2015 Atomic and molecular hydrogen gas temperatures in a low-pressure helicon plasma *Plasma Sources Sci. Technol.* **24** 045003

[49] Rauner D, Kurutz U and Fantz U 2015 Comparison of measured and modelled negative hydrogen ion densities at the ECR-discharge HOMER p 020017

[50] Béchu S, Aleiferis S, Bentounes J, Gavilan L, Shakhatov V A, Bès A, Svarnas P, Mazouffre S, de Oliviera N, Engeln R and Lemaire J L 2017 Detection of rovibrationally excited molecular hydrogen in the electronic ground state via synchrotron radiation *Appl. Phys. Lett.* **111** 074103

[51] Hiskes J R 1991 Cross sections for the vibrational excitation of the H_2 $X^1\Sigma^+_g(v)$ levels generated by electron collisional excitation of the higher singlet states *J. Appl. Phys.* **70** 3409

[52] Komppula J, Tarvainen O, Lätti S, Kalvas T, Koivisto H, Toivanen V and Myllyperkiö P 2013 VUV-diagnostics of a filament-driven arc discharge H^- ion source *AIP Conf. Proc.* **1515** 66–73

[53] Haas F A and Braithwaite N S J 1999 Tailoring of electron energy distributions in low-pressure inductive discharges *Appl. Phys. Lett.* **74** 338

[54] Haas F A, Goodyear A and Braithwaite N S J 1998 Tailoring of electron energy distributions in low temperature plasmas *Plasma Sources Sci. Technol.* **7** 471–7

[55] Tarvainen O and Peng S X 2016 Radiofrequency and 2.45 GHz electron cyclotron resonance H^- volume production ion sources *New J. Phys.* **18** 105008